www.sciencemag.org/content/354/6311/444/suppl/DC1

Supplementary Materials for

Direct frequency comb measurement of OD + CO → DOCO kinetics

B. J. Bjork,* T. Q. Bui, O. H. Heckl, P. B. Changala, B. Spaun, P. Heu, D. Follman, C. Deutsch, G. D. Cole, M. Aspelmeyer, M. Okumura, J. Ye*

*Corresponding author. Email: bryce.bjork@colorado.edu (B.J.B.); ye@jila.colorado.edu (J.Y.)

Published 28 October 2016, *Science* **354**, 444 (2016)
DOI: 10.1126/science.aag1862

This PDF file includes:

Supplementary Materials and Methods:

§1. Experimental description and conditions

Scientific Apparatus: A schematic of the instrument is depicted in Fig. S1 and discussed extensively in the main text.

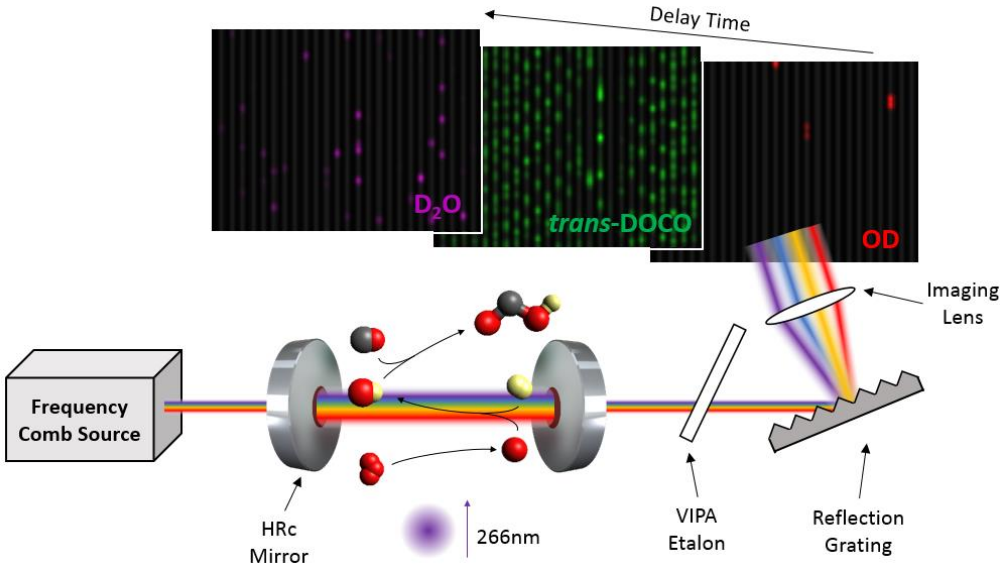

Fig. S1. A mid-IR frequency comb is coupled into an enhancement cavity, consisting of two high reflectivity crystalline (HRc) mirrors, where a 266 nm laser pulse photolyzes O_3 to initiate the chemistry. The transmission from the cavity is spatially dispersed by a VIPA etalon and a diffraction grating and imaged on an InSb camera. Simulated cavity absorbance images are shown for OD (red), *trans*-DOCO (green), and D_2O (magenta) to illustrate the camera pixel to wavelength mapping.

Generation of OD: The ozone used to generate OD in this reaction was generated in a flow-discharge of pure O_2 gas. This mixture contains approximately 8% of O_3 in a buffer of O_2. This mixture was flown across a silica gel trap immersed in an isopropanol/LN_2 bath at -90 °C.

The ozone trap was allowed to pump out for about 20 minutes after stopping the O_3/O_2 flow to remove residual O_2. The steady state concentration of O_3 in the reaction cell was measured using the direct absorption of the collimated 270 nm light from a UV LED (UVTOP-270). By comparing this absorption measurement to a static total pressure measurement in the cell, it is estimated that O_3 comprises >70% of the mixture flowing. Frequency quadrupled 266 nm light (beam size: 44 mm × 7 mm, power = 32mJ/pulse) from a Spectra Physics INDI-HG-105 Nd:YAG propagating orthogonal to the mid-IR probe beam was the photolysis beam. In this method, 15% of the O_3 in the cavity was photolyzed into $O(^1D)$, $O(^3P)$, and O_2 to start the reaction. OD was then promptly formed from the $O(^1D) + D_2 \rightarrow OD + D$ reaction.

O_3 photolysis to $O(^1D)$: In order to accurately simulate the kinetics of the OD + CO chemical system, we measured the fraction of O_3 photolyzed at 266 nm. This was done by measuring the transmission of a 270 nm LED through the photolysis region of the chemical cell before and after the photolysis of O_3 in a buffer of N_2. We measured a photolysis fraction of $f_{phot} = 0.15 \pm 0.02$.

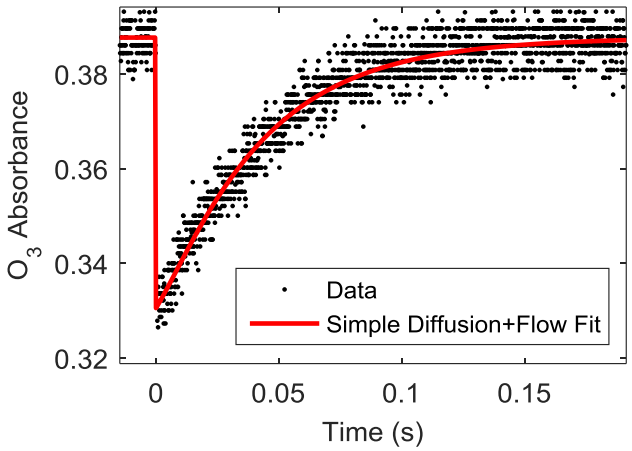

Fig. S2. Measurement of Ozone photolysis fraction.

Experimental conditions: Table S1 shows the measurement conditions used for determining k_{1a}. The initial concentrations of D_2, CO, N_2, and O_3 were determined by calibrated flow controllers and a capacitance manometer as

$$[N_2]_0 = P\left(\frac{Q_{N2}}{Q_{D2} + Q_{CO} + Q_{N2} + Q_{O3}}\right) \qquad \text{(S1)}$$

where P is the total pressure of the reaction cell and the Q_X are the flows of each gas into the reaction cell. By swapping flow controllers and pressure meters, the concentration uncertainty in this method is estimated to be 7%.

The initial concentrations of O_3, $O(^1D)$, and O_2 just after photolysis by the YAG beam are given by

$$\begin{aligned} [O_3]_0 &= (1 - f_{phot})[O_3]_{LED} \\ [O(^1D)]_0 &= q_{O(1D)}(f_{phot})[O_3]_{LED} \\ [O(^3P)]_0 &= q_{O(3P)}(f_{phot})[O_3]_{LED} \end{aligned} \qquad \text{(S2)}$$

where $q_{O(1D)} = 0.90$ and $q_{O(3P)} = 0.10$ are the quantum yields (*41*) of the photolysis of O_3 into $O(^1D)$ and $O(^3P)$, respectively, $f_{phot} = 0.15 \pm 0.02$ the O_3 photolysis fraction, and $[O_3]_{LED}$ is the steady-state concentration of O_3 recorded by the absorption of the 270 nm UV LED.

Table S1: Measurement conditions used for the determination of k_{1a}. The units for [CO], [N_2], [D_2], and [O_3] are molecules cm^{-3}.

	[CO]	[N_2]	[D_2]	[O_3]	Int. Time (μs)
CO Scan	7.41×10^{16}	8.89×10^{17}	2.96×10^{17}	1.00×10^{15}	50
	1.48×10^{17}	8.89×10^{17}	7.41×10^{16}	1.00×10^{15}	50
	2.96×10^{17}	8.89×10^{17}	7.41×10^{16}	1.00×10^{15}	10
	2.96×10^{17}	8.89×10^{17}	7.41×10^{16}	1.00×10^{15}	50
	5.92×10^{17}	8.89×10^{17}	7.41×10^{16}	1.55×10^{15}	10
	5.92×10^{17}	8.89×10^{17}	7.41×10^{16}	1.00×10^{15}	50
	5.92×10^{17}	8.89×10^{17}	7.41×10^{16}	1.00×10^{15}	50
	7.41×10^{17}	8.89×10^{17}	7.41×10^{16}	1.00×10^{15}	10
	7.41×10^{17}	8.89×10^{17}	7.41×10^{16}	1.00×10^{15}	50
	8.89×10^{17}	8.89×10^{17}	7.41×10^{16}	1.00×10^{15}	10
	9.63×10^{17}	8.89×10^{17}	7.41×10^{16}	1.00×10^{15}	10
	9.63×10^{17}	8.89×10^{17}	7.41×10^{16}	1.00×10^{15}	50
	1.18×10^{18}	8.89×10^{17}	7.41×10^{16}	1.00×10^{15}	10
	1.18×10^{18}	8.89×10^{17}	7.41×10^{16}	1.00×10^{15}	50
	1.18×10^{18}	8.89×10^{17}	7.41×10^{16}	1.00×10^{15}	50
	1.48×10^{18}	8.89×10^{17}	7.41×10^{16}	1.00×10^{15}	50
N_2 Scan	5.92×10^{17}	1.48×10^{17}	7.41×10^{16}	1.00×10^{15}	50
	5.92×10^{17}	2.96×10^{17}	7.41×10^{16}	1.00×10^{15}	50
	5.92×10^{17}	5.92×10^{17}	7.41×10^{16}	1.00×10^{15}	50
	5.92×10^{17}	7.41×10^{17}	7.41×10^{16}	1.00×10^{15}	50
	5.92×10^{17}	9.92×10^{17}	7.41×10^{16}	1.00×10^{15}	50
	5.92×10^{17}	1.18×10^{18}	7.41×10^{16}	1.00×10^{15}	50
	5.92×10^{17}	1.33×10^{18}	7.41×10^{16}	1.00×10^{15}	50
	5.92×10^{17}	1.33×10^{18}	7.41×10^{16}	1.00×10^{15}	50
	5.92×10^{17}	1.48×10^{18}	7.41×10^{16}	1.00×10^{15}	50
	5.92×10^{17}	1.48×10^{18}	7.41×10^{16}	1.00×10^{15}	50
O_3 Scan	1.48×10^{17}	8.89×10^{17}	7.41×10^{16}	5.00×10^{14}	50
	1.48×10^{17}	8.89×10^{17}	7.41×10^{16}	1.00×10^{15}	50
	1.48×10^{17}	8.89×10^{17}	7.41×10^{16}	2.50×10^{15}	50
	1.48×10^{17}	8.89×10^{17}	7.41×10^{16}	5.00×10^{15}	50
	2.96×10^{17}	8.89×10^{17}	9.57×10^{16}	1.00×10^{14}	50
	2.96×10^{17}	8.89×10^{17}	8.74×10^{16}	5.00×10^{14}	50
	2.96×10^{17}	8.89×10^{17}	7.41×10^{16}	1.00×10^{15}	50
	2.96×10^{17}	8.89×10^{17}	7.41×10^{16}	2.00×10^{15}	50
	2.96×10^{17}	8.89×10^{17}	8.15×10^{16}	5.00×10^{15}	50
D_2 Scan	2.96×10^{17}	8.89×10^{17}	1.48×10^{17}	1.00×10^{15}	50
	2.96×10^{17}	8.89×10^{17}	2.96×10^{17}	1.00×10^{15}	50

	2.96×10^{17}	8.89×10^{17}	5.92×10^{17}	1.00×10^{15}	50
	2.96×10^{17}	8.89×10^{17}	8.89×10^{17}	1.00×10^{15}	50
	2.96×10^{17}	8.89×10^{17}	1.18×10^{18}	1.00×10^{15}	50
OD(v=1) lifetime	0	9.98×10^{17}	8.32×10^{16}	1.00×10^{16}	50
	2.06×10^{16}	9.91×10^{17}	8.26×10^{16}	1.00×10^{16}	50
	4.08×10^{16}	9.79×10^{17}	8.16×10^{16}	1.00×10^{16}	50
	5.64×10^{16}	9.67×10^{17}	8.06×10^{16}	1.00×10^{16}	50
	8.19×10^{16}	9.83×10^{17}	8.19×10^{16}	1.00×10^{16}	50
	9.79×10^{16}	9.80×10^{17}	8.17×10^{16}	1.00×10^{16}	50

§2. Data extraction & analysis

Spectral acquisition: The transmitted mid-IR light was spatially dispersed using a Virtually Imaged Phased Array (VIPA) and detected using a FLIR SC6000 InSb camera, in the same manner as Fleisher *et al.* (*23*). The camera integration (50 μs or 10 μs integration time) was synchronized to the Nd:YAG photolysis pulse. A digital delay generator sets the variable delay times from the photolysis pulse. Since we are not resolving individual frequency comb modes, we calibrated our frequency axis each day to known D_2O line positions from Ref. (*37*).

The experiment was conducted at a 10 Hz repetition rate, set by the maximum repetition rate of the pulsed Nd:YAG laser. A "reference" image was collected directly prior to each Nd:YAG pulse and "signal" images were collected at various delay times following the Nd:YAG pulse. Since the InSb camera has a dark current offset that drifts with ambient temperature, a "background" image was also collected at the same repetition rate by briefly blocking the camera with an optical shutter.

After collecting each set of images, the absorbance was constructed in the following manner

$$A = -\log\left(\frac{S-B}{R-B}\right), \qquad \text{(S3)}$$

where *S*, *R*, and *B* are the signal, reference, and background images, respectively. Due to slowly-varying baseline fluctuations in the transmission through the cavity, a sliding average was subtracted from the measured absorbance as a function of wavenumber, forming a "high-passed" signal $\tilde{A} = A - H[A]$, where *H* is the sliding average function. Following the "high-pass" filter operation, the error at each point in the spectrum is estimated by taking the standard deviation of the surrounding points. In this manner, each collected spectrum is assigned a value and error corresponding to $\tilde{A} \pm \delta\tilde{A}$. Averaging many of these values yields an average value $\tilde{A}_{mean} \pm \delta\tilde{A}_{mean}$. Since this "sliding standard deviation" operation includes some of the absorption peaks in the spectrum, it is a slight overestimate of the error in the spectrum.

Spectral fitting: In direct absorption spectroscopy, the concentration of a species is related to the transmission of a probe beam through the relation

$$\frac{I_S(\tilde{\nu})}{I_R(\tilde{\nu})} = e^{-n\sigma(\tilde{\nu})l}, \qquad \text{(S4)}$$

where $I_S(\tilde{\nu})$ and $I_R(\tilde{\nu})$ are the light intensities with and without the sample, n is the molecular concentration in molecules cm^{-3}, $\sigma(\tilde{\nu})$ is the molecular absorption cross section in cm^2, l is the path length through the sample in cm, and $\tilde{\nu}$ is wavenumber in cm^{-1}. For this experiment, $I_R(\tilde{\nu})$ is recorded 4 ms before the photolysis pulse and $I_S(\tilde{\nu})$ is recorded after the photolysis pulse by the InSb camera. If multiple species are present, the transmission versus time is now given by

$$-\frac{1}{l}\log\left(\frac{I_S(\tilde{\nu})}{I_R(\tilde{\nu})}\right) = n_{\mathrm{A}}(t)\sigma_{\mathrm{A}}(\tilde{\nu}) + n_B(t)\sigma_B(\tilde{\nu}) + \ldots, \qquad \text{(S5)}$$

where A and B are two sample molecules. If $\sigma_{\mathrm{A}}(\tilde{\nu})$, $\sigma_B(\tilde{\nu})$ are linearly independent as a function of wavelength, then $n_{\mathrm{A}}(t)$, $n_{\mathrm{B}}(t)$ are determined uniquely through linear regression. $\sigma(\tilde{\nu})$ is related to the molecular line strength S through $\sigma(\tilde{\nu}) = Sg(\tilde{\nu} - \tilde{\nu}_0)$ where $g(\tilde{\nu} - \tilde{\nu}_0)$ is the area normalized lineshape function. In our case, $g(\tilde{\nu} - \tilde{\nu}_0)$ is a Gaussian function with FWHM = 900 MHz. This is significantly larger than the molecular Doppler width, so convolution with the molecular lineshape is neglected.

Since we "high-pass" the measured absorbance, $A(\tilde{\nu})$, to reduce the effects of cavity fluctuations, it is also necessary to perform the same operation on the calculated molecular cross sections. This will not affect the fitted concentration values, since the sliding average operation $H[A]$ is a linear function and thus

$$-\frac{1}{l}\log\left(A - H[A]\right) = n_{\mathrm{A}}(t)(\sigma_{\mathrm{A}}(\tilde{\nu}) - \mathrm{H}[\sigma_{\mathrm{A}}(\tilde{\nu})]) + n_{\mathrm{B}}(t)(\sigma_{\mathrm{B}}(\tilde{\nu}) - \mathrm{H}[\sigma_{\mathrm{B}}(\tilde{\nu})]) + \ldots, \qquad \text{(S6)}$$

where A is the absorbance, given by $A = -\log\left(\frac{I_S(\tilde{\nu},t)}{I_R(\tilde{\nu})}\right)$.

Spectral line intensities: Experimental details for obtaining line positions and line intensities for D_2O are found in Ref. (*37*) and Ref. (*42*), respectively. Unpublished line intensities (Table S2) measured by Dr. Robert A. Toth using a Fourier transform spectrometer(*37*) are generously provided through private communication with Dr. Keeyoon Sung of JPL. Line positions for OD(v=0,1) were obtained from Ref. (*36*). PGopher (*34*) was used along with fit parameters from Ref. (*36*) to obtain relative line strengths for each line in the spectrum. The OD

v=0 and v=1 transition dipole moments $|\mu^{OD}_{0\rightarrow1}| = 0.0303$ and $|\mu^{OD}_{1\rightarrow2}| = 0.0386$ D were obtained from mass-scaling the OH transition dipole moments. The $|\mu^{OH}_{0\rightarrow1}| = 0.0343$ and $|\mu^{OH}_{1\rightarrow2}| = 0.0408$ transition dipole moments were calculated using the RKR potential and dipole moment functions reported by Nesbitt and coworkers (*43, 44*). The error in the transition dipole moments is estimated to be <10% for OD. *trans*-DOCO ν_1 ro-vibrational parameters were obtained from Ref. (*35*) and used to simulate the ro-vibrational spectrum in PGopher. As there are no known measurements of the *trans*-DOCO band intensity, we assume a *trans*-DOCO ν_1 band strength of $S_{trans\text{-DOCO}} = 65 \pm 5$ km/mol, estimated from a series of anharmonic VPT2 vibrational calculations performed at the CCSD(T)/ANOn (n = 0,1,2) and CCSD(T)/cc-pCVXZ (X = D,T,Q) levels of theory (personal communication with J. F. Stanton).

Table S2: D_2O line positions and intensities from Toth et al. (*37*). Note that only the line positions are published, whereas the line intensities are provided through private communication with Dr. Keeyoon Sung of JPL.

Line Position (cm^{-1})	Line Intensity [cm^{-1}/(molecule × cm^{-2})]	Line Position (cm^{-1})	Line Intensity [cm^{-1}/(molecule × cm^{-2})]	Line Position (cm^{-1})	Line Intensity [cm^{-1}/(molecule × cm^{-2})]
2640.2345	2.64×10^{-22}	2649.42945	4.41×10^{-21}	2658.5228	3.42×10^{-22}
2640.4272	5.23×10^{-22}	2649.5656	6.13×10^{-23}	2659.1482	1.12×10^{-20}
2641.2913	7.85×10^{-24}	2649.6475	2.37×10^{-23}	2659.9311	1.12×10^{-23}
2641.53603	7.85×10^{-24}	2649.86673	4.86×10^{-21}	2660.1669	1.86×10^{-23}
2642.3123	2.93×10^{-21}	2650.0932	1.2×10^{-21}	2660.57108	4.45×10^{-23}
2642.6734	1.23×10^{-21}	2650.24288	6.78×10^{-21}	2660.7399	3.8×10^{-21}
2643.143	1.38×10^{-22}	2650.52625	3.82×10^{-23}	2661.1383	1.88×10^{-23}
2643.5818	3.23×10^{-22}	2650.61934	2.61×10^{-21}	2661.1527	3.81×10^{-23}
2643.59308	1.27×10^{-23}	2651.0157	1.19×10^{-23}	2661.3546	3.61×10^{-23}
2643.9221	1.73×10^{-21}	2652.1988	1.18×10^{-21}	2661.55001	4.41×10^{-21}
2643.99044	2.82×10^{-21}	2652.7398	2.55×10^{-23}	2661.7319	1.36×10^{-22}
2644.2378	8.58×10^{-24}	2652.8054	7.44×10^{-22}	2663.6125	2.79×10^{-21}
2644.4066	4.29×10^{-24}	2652.8692	3.71×10^{-22}	2663.6323	5.43×10^{-21}
2644.566	6.46×10^{-23}	2654.5461	2.49×10^{-21}	2663.91535	3.88×10^{-21}
2644.6401	3.64×10^{-22}	2654.5589	2.66×10^{-21}	2664.1152	1.13×10^{-21}
2644.7931	8.58×10^{-24}	2655.2742	1.56×10^{-22}	2664.25555	3.61×10^{-21}
2645.1625	2.66×10^{-24}	2655.299	1.01×10^{-22}	2664.4722	1.83×10^{-23}
2645.335	7.64×10^{-22}	2655.7285	1.25×10^{-21}	2664.9705	4.49×10^{-22}
2645.7443	4.41×10^{-22}	2655.8308	7.93×10^{-23}	2664.98852	9.44×10^{-22}
2646.18699	1.9×10^{-21}	2655.928	4.41×10^{-23}	2665.9744	5.8×10^{-23}
2646.68677	2.39×10^{-21}	2657.027	1.13×10^{-23}	2666.5308	1.35×10^{-22}
2646.723	3.85×10^{-21}	2657.1548	5.48×10^{-24}	2666.99383	7.97×10^{-21}
2647.0682	2.12×10^{-21}	2657.4666	3.44×10^{-23}	2667.1147	7.27×10^{-23}
2647.205	1.57×10^{-21}	2657.52565	8.09×10^{-21}	2667.2057	2.58×10^{-21}
2647.34975	4.17×10^{-21}	2657.7129	3.81×10^{-21}	2668.64249	6.78×10^{-21}
2647.3844	1.63×10^{-23}	2657.848	4.37×10^{-23}	2668.91278	1.14×10^{-20}
2648.28	6.95×10^{-21}	2658.12175	3.91×10^{-22}	2669.2846	1.28×10^{-23}
2649.043	1.01×10^{-22}	2658.20235	3.58×10^{-21}	2669.5047	4.45×10^{-22}
2649.061	7.03×10^{-24}	2658.2584	1.99×10^{-22}	2670.13472	5.56×10^{-21}
2649.0898	1.5×10^{-23}	2658.3467	2.37×10^{-23}	2670.54029	5.11×10^{-23}

Line Position (cm^{-1})	Line Intensity [cm^{-1}/(molecule × cm^{-2})]	Line Position (cm^{-1})	Line Intensity [cm^{-1}/(molecule × cm^{-2})]	Line Position (cm^{-1})	Line Intensity [cm^{-1}/(molecule × cm^{-2})]
2670.8972	7.68×10^{-23}	2682.7988	3.24×10^{-21}	2693.6488	1.25×10^{-21}
2670.9733	1.57×10^{-22}	2683.0851	6.7×10^{-23}	2694.1202	2.49×10^{-22}
2671.5212	5.43×10^{-23}	2684.0578	1.64×10^{-22}	2694.23385	4.01×10^{-23}
2671.5883	4.07×10^{-22}	2684.16277	9.19×10^{-21}	2695.3701	1.53×10^{-21}
2671.6725	2.78×10^{-23}	2684.4509	3.24×10^{-21}	2695.516	1.57×10^{-22}
2671.7708	2.28×10^{-23}	2684.5865	4.29×10^{-23}	2695.9146	2.17×10^{-21}
2671.91013	1.38×10^{-23}	2685.00147	2.82×10^{-23}	2696.25256	2.14×10^{-20}
2672.1342	1.73×10^{-23}	2685.2205	1.56×10^{-23}	2696.4641	7.48×10^{-23}
2672.3234	1.27×10^{-20}	2685.4227	3.61×10^{-23}	2696.8033	1.57×10^{-24}
2672.4246	1.25×10^{-22}	2685.7946	7.56×10^{-23}	2697.27755	1.75×10^{-21}
2672.57006	2.55×10^{-23}	2686.09833	5.31×10^{-23}	2697.3128	1.54×10^{-22}
2672.71	1.18×10^{-22}	2686.79348	1.35×10^{-21}	2697.6058	1.5×10^{-22}
2672.7446	1.92×10^{-22}	2686.986	7.48×10^{-23}	2697.7648	1.12×10^{-23}
2672.771	7.36×10^{-23}	2688.01359	7.97×10^{-23}	2697.81728	2.3×10^{-23}
2672.81345	3.01×10^{-23}	2688.5288	3.08×10^{-21}	2698.6272	3.69×10^{-22}
2674.1562	3×10^{-24}	2688.55586	5.97×10^{-21}	2699.0851	1.26×10^{-21}
2674.2478	8.74×10^{-23}	2688.7263	2.68×10^{-23}	2699.09974	9.4×10^{-22}
2675.0847	8.99×10^{-23}	2688.82239	7.64×10^{-21}	2699.39049	4.29×10^{-23}
2675.359	1.17×10^{-22}	2689.0089	1.49×10^{-21}	2700.0094	2.73×10^{-23}
2676.21568	5.27×10^{-21}	2689.3199	2.47×10^{-22}	2700.0249	2.38×10^{-22}
2676.3165	2.67×10^{-21}	2689.4355	2.21×10^{-24}	2700.1138	8.54×10^{-22}
2676.47655	4.7×10^{-23}	2689.90787	2.63×10^{-20}	2700.1409	6.95×10^{-22}
2676.6666	1.25×10^{-21}	2690.1185	4.82×10^{-22}	2700.4127	1.79×10^{-20}
2676.999	1.44×10^{-22}	2690.4366	1.1×10^{-22}	2700.485	5.8×10^{-22}
2677.5985	1.75×10^{-20}	2690.8628	1.52×10^{-24}	2700.62468	7.97×10^{-21}
2678.22986	1.03×10^{-20}	2691.1606	1.36×10^{-20}	2700.8671	7.44×10^{-22}
2679.5902	5.07×10^{-21}	2691.46408	8.74×10^{-23}	2701.0039	1.29×10^{-21}
2679.8475	6.5×10^{-23}	2691.6066	1.98×10^{-21}	2701.1606	5.6×10^{-23}
2679.9658	1.81×10^{-22}	2691.69857	6.46×10^{-21}	2701.24658	3.5×10^{-20}
2680.3429	2.01×10^{-20}	2691.7401	1.21×10^{-20}	2701.4495	8.54×10^{-23}
2680.55718	9.19×10^{-21}	2691.91439	1.09×10^{-20}	2702.01668	1.88×10^{-20}
2680.60718	1.88×10^{-20}	2691.993	2.27×10^{-22}	2702.447	1.51×10^{-22}
2680.83526	1.75×10^{-20}	2692.10628	1.37×10^{-24}	2702.635	2.64×10^{-22}
2680.8799	3.58×10^{-23}	2692.26094	1.29×10^{-20}	2702.6618	5.48×10^{-23}
2681.1146	1.48×10^{-23}	2692.49856	1.79×10^{-20}	2702.76315	1.14×10^{-22}
2681.8938	1.32×10^{-21}	2692.7442	4.25×10^{-23}	2702.79603	3.43×10^{-20}
2682.04028	7.23×10^{-23}	2692.7624	1.53×10^{-20}	2703.0353	1.25×10^{-21}
2682.44429	3.66×10^{-23}	2693.22996	2.42×10^{-24}	2703.1091	5.48×10^{-23}

Line Position (cm^{-1})	Line Intensity [cm^{-1}/(molecule × cm^{-2})]	Line Position (cm^{-1})	Line Intensity [cm^{-1}/(molecule × cm^{-2})]
2704.74772	1.39×10^{-20}	2717.5068	5.35×10^{-21}
2704.8754	7.52×10^{-22}	2717.55131	1.06×10^{-20}
2704.93343	6.95×10^{-21}	2717.7698	8.3×10^{-22}
2705.52613	4.99×10^{-21}	2718.0281	8.09×10^{-24}
2705.7734	2.5×10^{-24}	2718.12162	7.11×10^{-24}
2705.86502	3.45×10^{-20}	2718.3284	3.37×10^{-22}
2705.993	1.25×10^{-22}	2719.1755	2.1×10^{-22}
2706.17996	2.62×10^{-20}	2719.52848	2.19×10^{-20}
2706.744	1.12×10^{-24}	2720.0076	1.36×10^{-20}
2706.86418	6.13×10^{-22}		
2707.1581	4.66×10^{-22}		
2708.56546	1.31×10^{-20}		
2708.6163	8.05×10^{-22}		
2709.2377	3.24×10^{-21}		
2709.312	3.72×10^{-22}		
2710.24857	6.5×10^{-22}		
2710.57106	3.32×10^{-21}		
2710.7739	9.85×10^{-22}		
2711.0795	5.43×10^{-22}		
2711.21661	4.29×10^{-20}		
2712.35984	2.37×10^{-20}		
2712.45137	4.41×10^{-20}		
2712.5763	8.99×10^{-22}		
2713.3275	3.79×10^{-23}		
2713.37758	8.17×10^{-23}		
2713.48368	1.27×10^{-22}		
2713.6902	1.89×10^{-23}		
2713.7529	3.19×10^{-22}		
2714.0415	1.99×10^{-20}		
2714.63906	1.12×10^{-22}		
2715.016	9.52×10^{-22}		
2715.6114	5.23×10^{-22}		
2715.8032	5.19×10^{-22}		
2715.835	2.41×10^{-22}		
2715.9995	1.03×10^{-21}		
2716.4458	4.33×10^{-22}		
2716.8877	1.73×10^{-21}		
2717.26396	4.29×10^{-23}		

Photolysis Path Length and Finesse: In cavity-enhanced spectroscopy, the path length l is given by the physical path length multiplied by a factor of $\beta F/\pi$, where F is the finesse of the optical cavity and $1 \leq \beta \leq 2$ is a parameter that arises when a sweep-lock is used (*45*). In addition, the path length is reduced to the width of the photolysis beam, l_{phot}. Thus, the effective optical absorption path length is given by

$$l_{eff} = \frac{\beta F l_{phot}}{\pi} . \qquad \text{(S7)}$$

The cavity finesse F as a function of wavelength was measured using cavity ringdown (Fig. S3).

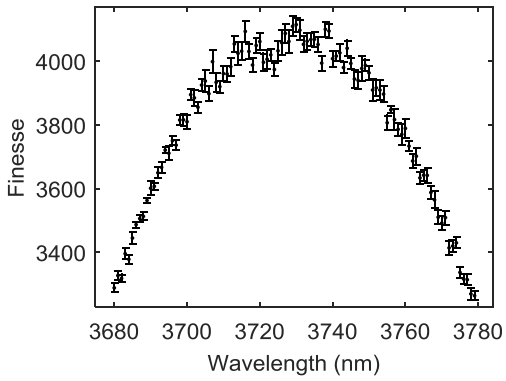

Fig. S3. Finesse from spectrally resolved cavity-ringdown measurements.

The photolysis path length, l_{phot}, was determined in two ways: (1) The width (46 ± 5 mm) of the burn spot on a photographic film from YAG beam, and (2) a razor blade scan across the beam and fitting the OD concentration at each point of the scan (Fig. S4). The razor blade method gave a beam width of 42 ± 4 mm, which is in agreement with the photographic film method. The weighted average of these two methods is 44 ± 3 mm.

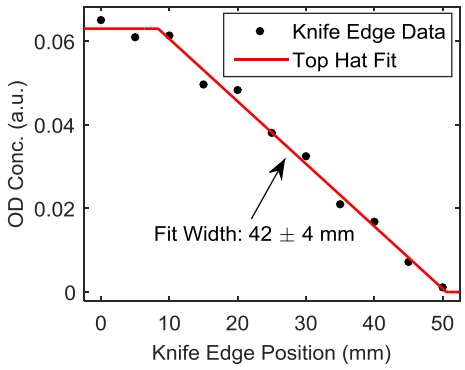

Fig. S4. Knife edge scan of YAG beam.

The error in the effective path length is given as

$$\delta l_{eff} = l_{eff}\sqrt{\left(\frac{\delta\beta}{\beta}\right)^2+\left(\frac{\delta F}{F}\right)^2+\left(\frac{\delta l_{phot}}{l_{phot}}\right)^2}\,, \qquad \text{(S8)}$$

which yields l_{eff} = 58±4 m at the finesse peak of 3725 nm.

Flow cell gas residence time: To ensure that fresh gas is introduced into the kinetics cell prior to each photolysis pulse, we measured the residence time by monitoring the D_2O stable product at our flow conditions. Fig. S5A shows the D_2O temporal profile at a few CO concentrations, along with a semi-empirical fit for estimating the gas half-life in our flow cell. $[D_2O](t)$ was fit to $[D_2O](t) = A(1-\alpha e^{-b_1 t} - (1-\alpha)\alpha e^{-b_2 t})e^{-b_{fall}t^2}$, where the rise of D_2O is expected to be bi-exponential and the fall is expected to be determined by the spatial profile of the YAG beam as well as diffusion dynamics. We determine the half-life of the cell by setting the fall function to 50%, which yields $\tau_{1/2} = \sqrt{\frac{\ln(2)}{b_{fall}}}$. This parameter is plotted as a function of [CO] in Fig. S5B. Since we do not see a systematic variation of the pump out time with [CO], we use the mean, 20.1±0.5 ms, as an estimate of the gas half-life for all conditions. Inserting this back into

the pump out function, we estimate that <1% of residual gas remains between photolysis pulses, separated by 100 ms.

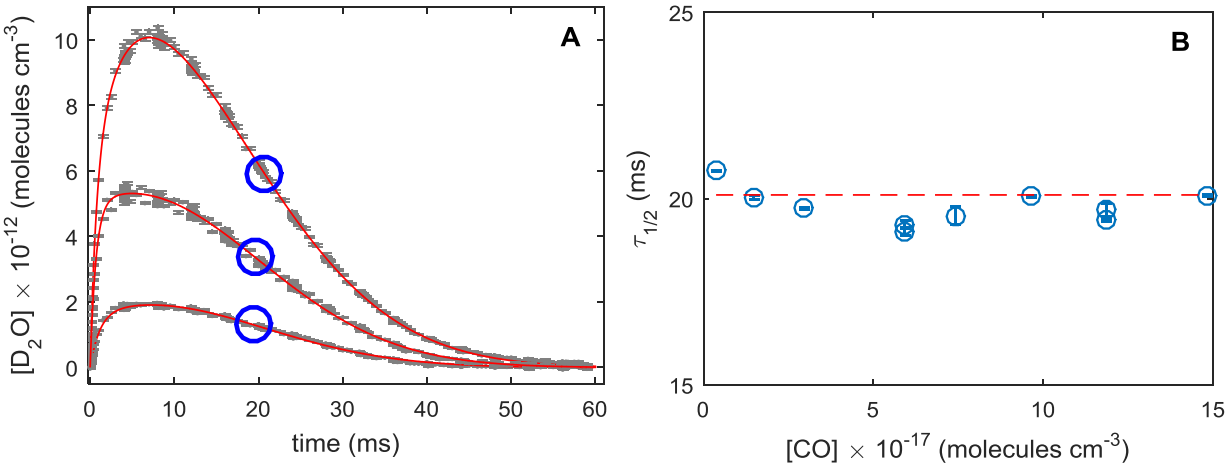

Fig. S5. **(A)** Experimental $[D_2O](t)$ (grey dots) for a few CO concentrations, along with temporal fits (red lines), which yield its half-life in the kinetics cell (blue circles). **(B)** D_2O half-life is plotted as a function of [CO] (blue circles). The mean of these values is indicated by a red dashed line.

§3. Sources of error

Spectral interference from D_2O: In performing a linear spectral fit to OD, D_2O, and *trans*-DOCO, it is possible that absorption from one species may interfere with another. This cross-contamination effect can be exacerbated if the lineshape of the fit does not exactly match the experiment. The largest cross-contamination effect in our experiment is between OD and D_2O, since half of the OD lines in our spectral window are contaminated by strong D_2O transitions. However, this is nearly negligible in the first 100 μs, where D_2O concentrations are low. Based on a comparison of contaminated and uncontaminated OD absorption features, we estimate that the systematic error due to cross-contamination is <1%.

Initial Rate Method: At early times, we expect DOCO to behave according to the first-order differential equation,

$$[\mathrm{DOCO}](t) = k_{1a}[\mathrm{CO}][\mathrm{OD}](t) - k_{loss}[\mathrm{X}] \ , \qquad \text{(S9)}$$

where [X] is the primary loss partner for DOCO and [OD](t) refers to the time-dependent concentration of OD in the ground vibrational state, OD(v=0). With the initial condition that [DOCO(t=0)] = 0, we can solve this equation directly for [DOCO](t) in terms of [OD](t), which yields

$$[\mathrm{DOCO}](t) = k_{1a}[\mathrm{CO}]\int_0^t e^{-(k_{loss}[\mathrm{X}])(t-u)}[\mathrm{OD}](u)du \ . \qquad \text{(S10)}$$

To obtain an analytic form for [OD](t), we fit a sum of exponentials to our experimental data, constrained by [OD](t=0) = 0.

$$[\mathrm{OD}](t) = a_1 e^{-b_1 t} + a_2 e^{-b_2 t} - (a_1 + a_2)e^{-b_3 t} \ . \qquad \text{(S11)}$$

Here, b_1 and b_2 are bi-exponential decay terms while b_3 is a rise term. The b_3 rise term for OD(v=0) is directly related to the decay of OD(v=1) where it originates. OD(v=1) decay will be discussed in more detail in the following sections. Using this expression for OD(t), DOCO(t) is given by:

$$[\mathrm{DOCO}](t) = k_{1a}[\mathrm{CO}]\left(a_1 \frac{e^{-b_1 t} - e^{-r_{loss} t}}{b_1 - r_{loss}} + a_1 \frac{e^{-b_2 t} - e^{-r_{loss} t}}{b_2 - r_{loss}} - (a_1 + a_2)\frac{e^{-b_3 t} - e^{-r_{loss} t}}{b_3 - r_{loss}} \right). \quad \text{(S12)}$$

DOCO(t) contains two free parameters in this expression, k_{1a}, and r_{loss} ($\equiv k_{loss}[\mathrm{X}]$). We fit a $r_{loss,exp}$ = (4.0±0.4)×10^4 s^{-1} to all data with constant [O_3], while our fit value of k_{1a} varies with N_2 and CO.

From our fit values of the bimolecular rate constant k_{1a}, we determine the termolecular rates $k_{1a}^{(CO)}$ and $k_{1a}^{(N2)}$ from a multidimensional linear regression to the expression

$$k_{1a} = k_{1a}^{(CO)}[CO] + k_{1a}^{(N2)}[N_2]. \qquad \text{(S13)}$$

The statistical error in our values of $k_{1a}^{(CO)}$ and $k_{1a}^{(N2)}$ are established from the variation in the fit residuals.

Uncertainty in the Initial Rate Method: To investigate the variation in our fitted k_{1a} values with integration time, we divided our values for k_{1a} (see main text) for 50 and 10 μs and plotted these values as a function of CO concentration. We display this value, $r = \frac{k_{1a,10\mu s}}{k_{1a,50\mu s}}$, with CO in Fig. S6.

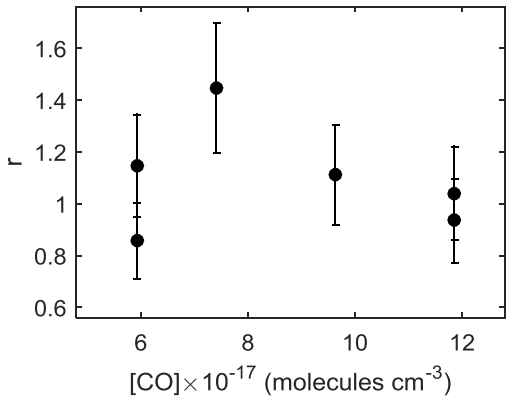

Fig. S6. The ratio of retrieved k_{1a} values for 50 μs and 10 μs integration times.

In order to estimate a general systematic error in a given data set, we calculate the weighted mean and standard deviation of this data, which are $\bar{r} = 1.09$ and $\sigma_r = 0.21$, respectively. We interpret $\bar{r} - 1 = 9\%$ as a systematic shift due to our 50 μs integration time and σ_r as an estimate of the statistical variation of k_{1a} with respect to integration time and [CO].

Effect of OD Vibrational Excitation: Since vibrationally hot OD(v>0) was generated under our experimental conditions, we investigated the effect of vibrational quenching of hot OD under conditions relevant for fitting the OD + CO → DOCO rate. First, $O(^1D) + D_2 \rightarrow OD + D$ promptly produces excited OD up to the 4th vibrational state (*46*). The second reaction, $D + O_3 \rightarrow OD + O_2$, continually generates hot OD up to the 9th vibrational state (*47*).

Due to the broad bandwidth and high sensitivity of our kinetics apparatus, we were simultaneously able to detect OD(v=0) and OD(v=1) in a time-resolved manner during each experimental run. Fig. S7 show an acquired spectrum containing both strong OD(v=0) (blue) and OD(v=1) (red) transitions.

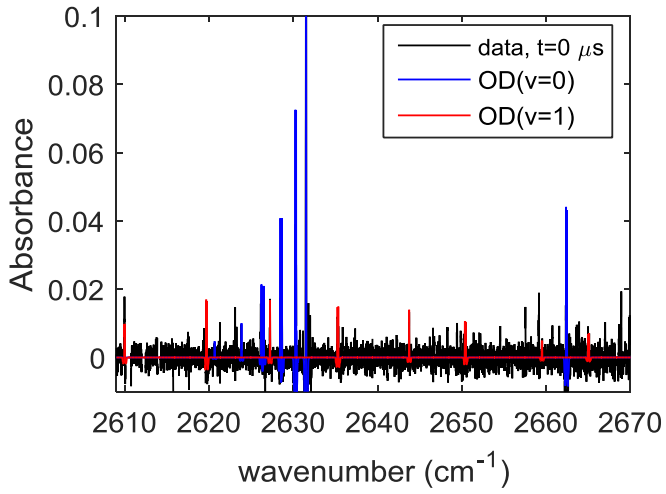

Fig. S7. Representative spectrum of OD(v=0) and OD(v=1) for measuring [OD(v>0)].

To constrain the extent to which OD(v>0) introduces error into our overall determination of k_{1a}, we conducted experiments to measure both the density and lifetime of OD(v=1) over a range of CO densities. Experiments were conducted with $[O_3] = 1\times10^{16}$ molecules cm^{-3}, which provided an upper limit for the vibrationally excited OD population. [CO] ranged from 0-9×10^{16} molecules cm^{-3}, which is well below the lowest [CO] used in our k_{1a} measurement. We observed high signal-

to-noise ratio OD(v=1) transitions, but not any OD(v>1), indicating that either 1) the densities are too low and/or 2) the lifetimes are too short for higher exited states. The results from this experiment are shown in Fig S8. At our operating conditions for determining k_{1a}, the lifetime of OD(v=1) is <5 μs. The measured densities for OD(v=1) are also <10% of OD(v=0). Therefore, even if OD(v>0) forms ground state *trans*-DOCO at the same rate as OD(v=0), this would only introduce a <10% uncertainty in our measurement, which has been included in our systematic error budget (Table S4).

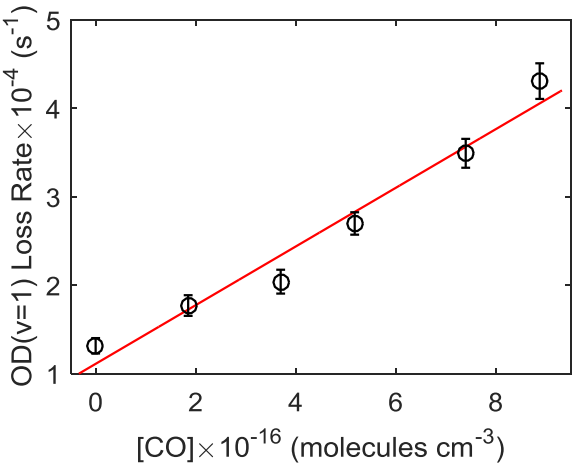

Fig. S8. First order decay rate of OD(v=1) as a function of [CO]. The fitted rate constant for OD(v=1) loss is (3.3±0.2)×10^{-13} cm^3 $molecules^{-1}$ s^{-1}.

OD(v=1) loss is due, at least in part, to quenching to ground state OD(v=0). The equation for [OD(v=0)](*t*), given by eq. S11, is used to fit [OD](*t*) as a function of [CO]. In eq. S11, the fitted parameter b_3, which describes the rise rate of OD, is plotted as a function of [CO] in Fig. S9. The fitted slope yields a rise rate constant for OD(v=0) of (3.8±0.5)×10^{-13} cm^3 $molecule^{-1}$ s^{-1}, which is slightly larger than our measured OD(v=1)+CO loss rate, (3.3 ± 0.2)×10^{-13} cm^3 $molecule^{-1}$ s^{-1}. This is expected since OD(v=2) → OD(v=1) quenching competes with OD(v=1) → OD(v=0) loss.

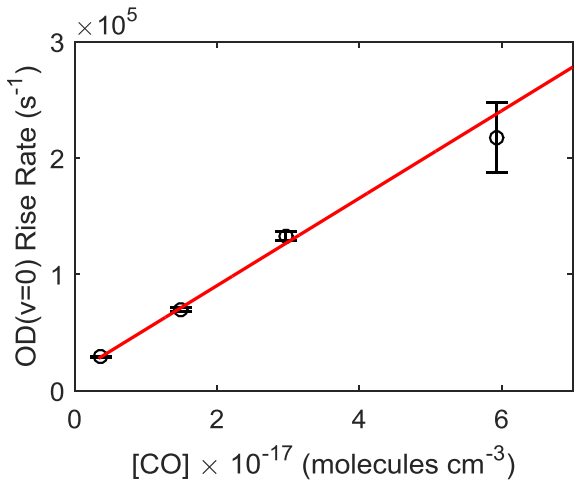

Fig. S9. OD(v=0) rise as a function of [CO]. The fitted rate constant for OD(v=0) rise is $(3.8\pm0.5)\times10^{-13}$ cm^3 molecule^{-1} s^{-1}.

Effect of D_2: In order to determine the systematic effects of large [D_2], we varied [D_2] under constant [N_2]=8.9×10^{17} molecules cm^{-3}, [CO] =3.0×10^{17} molecules cm^{-3}, and [O_3]=1.0×10^{15} molecules cm^{-3}. The results, shown in Fig. S10, show no statistically significant variation with [D_2]. While there are no literature estimates of the DOCO* + D_2 → DOCO + D_2 quenching efficiency, we might expect this rate to be slower than the N_2 rate by about a factor of 2, given similar comparisons in toluene (*48*). In this case, we would expect the termolecular rate k_{1a} to change by about 0.5×10^{14} cm^3 molecules^{-1} s^{-1} with a 1×10^{18} molecules cm^{-3} variation in [D_2]. The magnitude of the uncertainty in Fig. S10 is about 0.6×10^{14} cm^3 molecules^{-1} s^{-1}, and hence a termolecular D_2 effect, if it exists, is masked by the noise.

Ideally, k_{1a} is determined in the limit of [D_2] → 0. To determine the shift associated with nonzero D_2, we performed a linear fit to this data, resulting in a slope of $(1.3 \pm 0.8) \times 10^{-33}$ cm^6 molecules^{-2} s^{-1} and an offset of $(1.44 \pm 0.06) \times 10^{-14}$ cm^3 molecules^{-1} s^{-1}. At our typical operating concentration of [D_2] = 7.4×10^{16} molecules cm^{-3}, this results in a systematic shift of (0.7 ± 0.4)%.

However, this analysis assumes that k_{1a} is linear with D_2. As a much more conservative estimate of our systematic error, we use the mean-normalized standard deviation, $\frac{\sigma_{k_{1a}}}{\overline{k_{1a}}} = 8\%$, of the data in Fig. S10 as the fractional statistical error due to nonzero $[D_2]$.

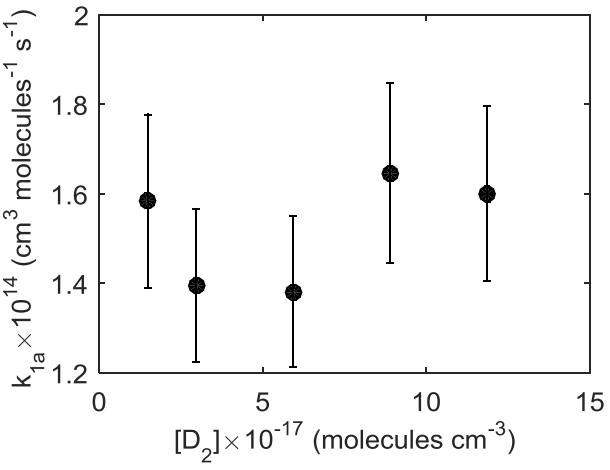

Fig. S10. Variation of k_{1a} with D_2 concentration.

Effect of O_3: In order to determine the systematic effects of $[O_3]$ in our measurement of $k_{1a}^{(CO)}$ and $k_{1a}^{(N2)}$, we varied $[O_3]$ under constant $[N_2]=8.9\times10^{17}$ molecules cm^{-3}, $[CO]=1.5\times10^{17}$ molecules cm^{-3}, and $[D_2]= 7.4\times10^{16}$ molecules cm^{-3}. With fixed $[O_3]=1\times10^{15}$ molecules cm^{-3}, we find our experimental data is consistent with a constant $r_{loss,exp} = (4.0\pm0.4)\times10^4$ s^{-1}, independent of $[N_2]$, $[D_2]$, and $[CO]$. In the case of varying $[O_3]$, however, we find that a constant $r_{loss,exp}$ term results in poor fits and also an observed systematic variation of k_{1a} with $[O_3]$. We therefore make the assumption that $r_{loss,exp}$ scales with $[O_3]$, i.e. $r_{loss,exp} = k_{O3}[O_3]$, where $k_{O3} = 4.0\times10^{-11}$ cm^3 molecules^{-1} s^{-1} is fixed by the results of the constant $[O_3]$ data. The retrieved values of k_{1a} vs $[O_3]$, shown in Fig. S11, display a weak dependence of k_{1a} on $[O_3]$. The weighted mean and standard deviation of this data are $\overline{k_{1a}} = 1.2\times10^{-14}$ cm^3 molecules^{-1} s^{-1} and $\sigma_{k1a} = 1.3\times10^{-15}$ cm^3 molecules^{-1} s^{-1}

, respectively. Ideally, k_{1a} is determined in the limit of $[O_3] \rightarrow 0$. Since we do not see a systematic variation of our retrieved k_{1a} value with $[O_3]$, we interpret $\frac{\sigma_{k_{1a}}}{\overline{k_{1a}}} = 11\%$ as a maximum statistical error due to nonzero $[O_3]$.

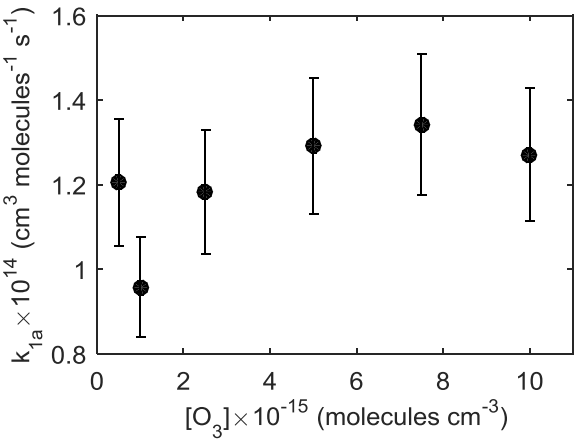

Fig. S11. Variation of k_{1a} with O_3 concentration.

§4. Rate Equation Model

A full rate equation model that includes all of the most relevant rates for the reaction of OD + CO is given in Table S3. The system of stiff differential equations was integrated using the SimBiology software package from MathWorks and also by the Kintecus software package (*49*), both of which were in strong agreement. As the experimental data were integrated over 50 or 10 μs, we also boxcar-averaged the results from the rate equation model to fit to experimental data.

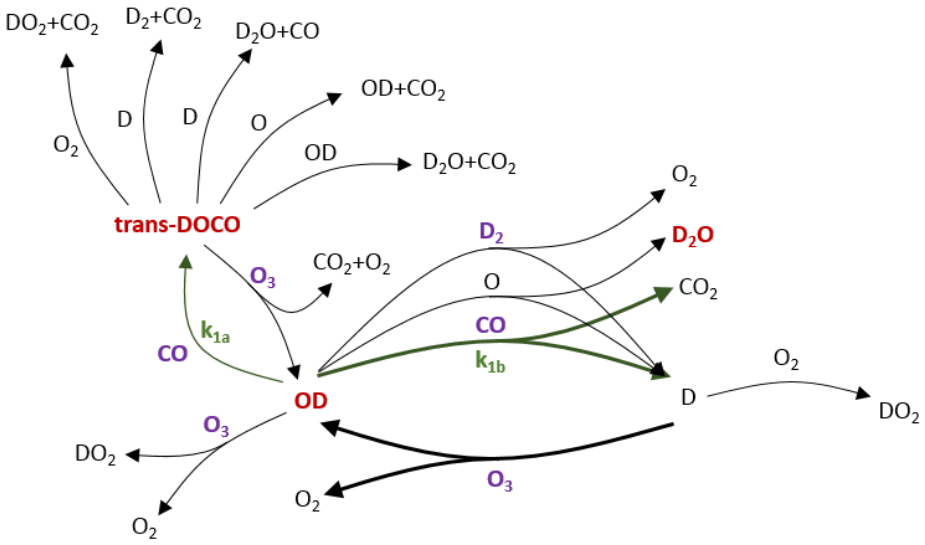

Fig. S12. Basic schematic of the rate equation model used in the present studies. Absolute time-dependent concentrations of the red molecules (*trans*-DOCO, OD(v=0), OD(v=1), and D_2O) are measured through cavity-enhanced absorption spectroscopy, while the concentrations of the precursors (purple) are fixed by controlling the flows of N_2, CO, and D_2 and measuring the UV absorption of O_3, respectively. The two relevant OD + CO branching reactions are indicated in green.

Table S3: Rates used for modelling the OD + CO reaction. Units for termolecular rates are cm^6 $molecules^{-2}$ s^{-1} and cm^3 $molecules^{-1}$ s^{-1} for k_0^{300} and k_∞^{300}, respectively.

Category	Reaction	Rate (cm^3 $molecules^{-1}$ s^{-1})	Source[1]	S_{OD} (%)	S_{DOCO} (%)	Ref(s)
$O(^1D)$ + X	$O(^1D) + N_2 \rightarrow O + N_2$	$(3.1 \pm 0.3) \times 10^{-11}$	DM	63	58	(*41*),(*50*)
	$O(^1D) + CO \rightarrow O + CO$	$(5.8 \pm 1.2) \times 10^{-11}$	DM	12	11	(*51*)
	$O(^1D) + O_2 \rightarrow O + O_2$	$(3.95 \pm 0.4) \times 10^{-11}$	DM	0	0	(*41*), (*52*)

	$O(^1D) + O_3 \rightarrow O_2 + O_2$	$(1.2 \pm 0.2) \times 10^{-10}$	DM	0	0	(*41*)
	$O(^1D) + O_3 \rightarrow O_2 + O + O$	$(1.2 \pm 0.2) \times 10^{-10}$	DM	0	0	(*41*)
	$O(^1D) + D_2 \rightarrow OD + D$	$(1.1 \pm 0.1) \times 10^{-10}$	DM	75	69	(*53*)
OD + X	$OD + O_3 \rightarrow DO_2 + O_2$	$(7.3 \pm 1.1) \times 10^{-14}$	DMH	1	1	(*41*),(*54*)
	$OD + D_2 \rightarrow D_2O + D$	$(1.65 \pm 0.13) \times 10^{-15}$	DM	1	1	(*55*)
	$OD + OD \rightarrow D_2O + O$	$(4.34 \pm 0.63) \times 10^{-13}$	DM	0	0	(*56*)
	$OD + DO_2 \rightarrow D_2O + O_2$	$(3.8 \pm 0.9) \times 10^{-11}$	DM	0	0	(*57*)
	$OD + D_2O_2 \rightarrow D_2O + DO_2$	$(5.91 \pm 0.42) \times 10^{-13}$	DM	0	0	(*58*)
	$OD + CO \rightarrow D + CO_2$	$(5.6 \pm 0.2) \times 10^{-14}$	DM	28	31	(*11, 14, 16, 39*)
	$OD + CO + N_2 \rightarrow DOCO + N_2$	**$(9.1 \pm 3.6) \times 10^{-33}$**				**(this work)**
	$OD + CO + CO \rightarrow DOCO + CO$	**$(2.0 \pm 0.8) \times 10^{-32}$**				**(this work)**
	$OD + OD \rightarrow D_2O_2$	Termolecular: $k_0^{300} = 6.9 \times 10^{-31}$ $k_\infty^{300} = 2.6 \times 10^{-11}$	DMH	0	0	(*41*)
	$O + OD \rightarrow O_2 + D$	$(3.3 \pm 0.5) \times 10^{-11}$	DMH	7	8	(*41*)
D + X	$D + O_3 \rightarrow OD + O_2$	$(2.9 \pm 0.3) \times 10^{-11}$	DMH	33	45	(*41*)
	$D + DO_2 \rightarrow OD + OD$	$(7.2 \pm 1.4) \times 10^{-11}$	DMH	0	0	(*41*)
	$D + DO_2 \rightarrow O + D_2O$	$(1.6 \pm 0.8) \times 10^{-12}$	DMH	0	0	(*41*)
	$D + DO_2 \rightarrow D_2 + O_2$	$(6.9 \pm 2.8) \times 10^{-12}$	DMH	0	0	(*41*)
	$D + O_2 \rightarrow DO_2$	Termolecular: $k_0^{300} = 4.4 \times 10^{-32}$ $k_\infty^{300} = 7.5 \times 10^{-11}$	DMH	0	0	(*41*)
DOCO + X	$DOCO + D \rightarrow D_2O + CO$	1.39×10^{-11}	TH	0	2	(*59*)

	$DOCO + O_3 \rightarrow OD + CO_2 + O_2$	$(4\pm0.4)\times10^{-11}$ (overall fit)	FIT	2	45	**(this work)**
	$DOCO + D \rightarrow D_2 + CO_2$	9.31×10^{-11}	TH	1	14	(*59*)
	$DOCO + OD \rightarrow D_2O + CO_2$	1.03×10^{-11}	TH	0	3	(*60*)
	$DOCO + O \rightarrow OD + CO_2$	1.44×10^{-11}	TH	0	8	(*61*)
	$DOCO + O_2 \rightarrow CO_2 + DO_2$	$(1.9 \pm 0.2) \times 10^{-12}$	DMH	0	3	(*62*)
	DOCO LOSS	(fitted for each trace)				
O + X	$O + O_3 \rightarrow O_2 + O_2$	$(8.0 \pm 0.8) \times 10^{-15}$	DM	0	0	(*41*)
	$O + DO_2 \rightarrow OD + O_2$	$(5.9 \pm 0.3) \times 10^{-11}$	DMH	1	0	(*41*)
	$O + D_2O_2 \rightarrow OD + DO_2$	$(1.7 \pm 0.3) \times 10^{-15}$	DMH	0	0	(*41*)
DO_2 + X	$DO_2 + O_3 \rightarrow OD + O_2 + O_2$	$(1.9 \pm 0.3) \times 10^{-15}$	DMH	0	0	(*41*)

[1] The source of the value used in the model is indicated: (TH) indicates a theoretical value, (DMH) indicates a direct experimental measurement of the Hydrogen-substituted reaction, and (DM) indicates a direct experimental measurement. (FIT) indicates a globally fitted reaction rate, specifically $DOCO + O_3$, which provided the best fit at $(4.0\pm0.4)\times10^{-11}$ cm^3 $molecule^{-1}$ s^{-1} for all scans.

Notes on Specific Reaction Rates:

$OD + CO \rightarrow D + CO_2$ This reaction rate was determined from the weighted average of three measurements from Paraskevopoulos *et al.* (*14*), Golden *et al.* (*11*), and Westenberg *et al.* (*39*). These values are $k_1 = (5.2\pm0.5)\times10^{-14}$, $(6.6\pm0.4)\times10^{-14}$, and $(5.48\pm0.2)\times10^{-14}$ cm^3 $molecules^{-1}$ s^{-1}, respectively. The result of the weighted average is $k_1 = (5.6\pm0.2)\times10^{-14}$ cm^3 $molecules^{-1}$ s^{-1}.

Sensitivity Analysis: In order to determine the sensitivity of the model on each of these parameters, a sensitivity analysis was done, measuring the variation of the DOCO and OD peak concentrations with each of the rate constants. The sensitivity, S_{DOCO}, is defined for a given rate constant k as

$$S_{DOCO} = \frac{k}{[\mathrm{DOCO}]_{max}} \frac{\partial [\mathrm{DOCO}]_{max}}{\partial k}, \qquad \text{(S14)}$$

where $[DOCO]_{max}$ is the maximum concentration of DOCO. S_{OD} is defined in a similar manner. These values essentially represent the fractional fluctuation of [DOCO] or [OD] with a fractional change in k. Values of these parameters are given in Table S3 for the conditions

$[O_3] = 1\times10^{15}$ molecules cm^{-3}

$[D_2] = 1\times10^{17}$ molecules cm^{-3}

$[CO] = 1\times10^{17}$ molecules cm^{-3}

$[N_2] = 1\times10^{18}$ molecules cm^{-3}.

Results of rate equation model fits: To compare the rate equation model to the experimental data, two parameters were fitted for each [OD](t), [DOCO](t) trace: an overall scaling factor for both OD and DOCO and a DOCO loss rate. Additionally, we found it necessary to fix the DOCO+O_3 rate as a constant and shared parameter for all traces, which yields a rate constant of 4×10^{-11} cm^3 $molecule^{-1}$ s^{-1}. The scaling factor accounts for uncertainties in both the effective optical path length and the OD* chemistry involved that establishes the initial OD concentration measured at steady-state. The results of these fits as a function of CO are shown in Fig. S13A-B. The averaged values for the overall scaling factor and the DOCO loss rate are

0.14±0.05 and (4.7±0.7)×10^3 s^{-1}, respectively. We observe a 65% correlation between the fitted overall scaling factor and DOCO loss rate.

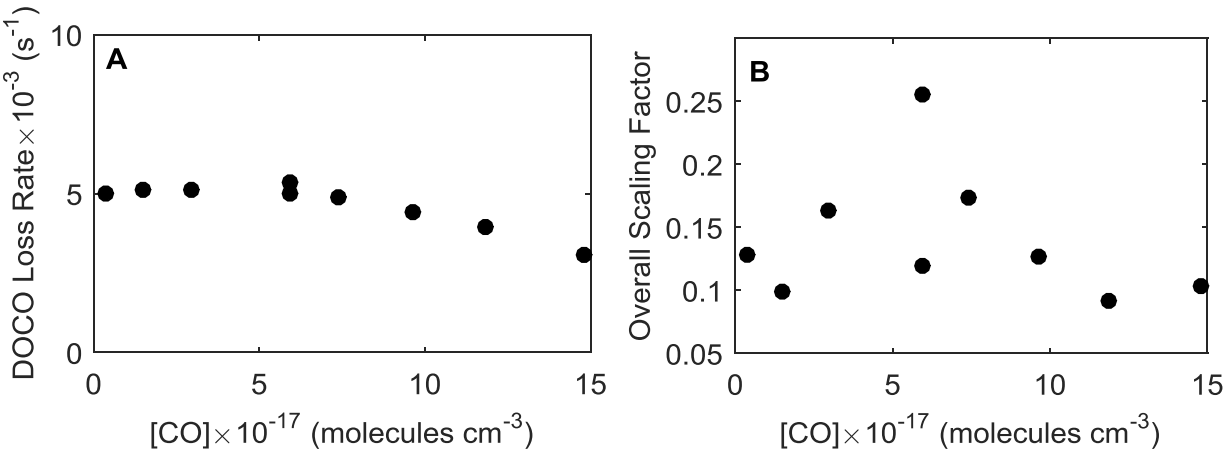

Fig. S13. Results of fitting the DOCO loss rate **(A)** and overall scaling factor **(B)** in the model to the data.

§5. Table of Statistical and Systematic Errors

Table S4: Summary of statistical and systematic errors

		Error Source	$k_{1a}^{(CO)}$	$k_{1a}^{(N2)}$
Statistical Errors		(statistical, from fit residual)	6%	10%
Experimental Control	**§1**	Flow & Pressure Measurement	7% (stat)	
Molecular Parameters	**§2**	OD Cross Section	10% (stat)	
	§2	DOCO Cross Section	10% (stat)	
Secondary Reactions	**§3**	Effect of D_2	8% (stat)	
	§3	Effect of O_3	11% (stat)	
Data Analysis	**§3**	Cross-contamination of OD and D_2O	-1% (sys)	
	§3	Effect of Integration Time	+9% (sys), 21% (stat)	
	§3	OD Vibrational Excitation	-10% (sys)	
		Total Systematic Error Budget	(-11%,+9%)	
		Total Statistical Error Budget	28%	29%
		Total Error Budget	(-39%,+37%)	(-40%,+38%)

References and Notes

1. A. W. Jasper, K. M. Pelzer, J. A. Miller, E. Kamarchik, L. B. Harding, S. J. Klippenstein, Predictive a priori pressure-dependent kinetics. *Science* **346**, 1212–1215 (2014). Medline doi:10.1126/science.1260856

2. T. L. Nguyen, B. C. Xue, R. E. Weston Jr., J. R. Barker, J. F. Stanton, Reaction of HO with CO: Tunneling is indeed important. *J. Phys. Chem. Lett.* **3**, 1549–1553 (2012). Medline doi:10.1021/jz300443a

3. J. S. Francisco, J. T. Muckerman, H. G. Yu, HOCO radical chemistry. *Acc. Chem. Res.* **43**, 1519–1526 (2010). Medline doi:10.1021/ar100087v

4. C. J. Johnson, R. Otto, R. E. Continetti, Spectroscopy and dynamics of the HOCO radical: Insights into the OH + CO → H + CO_2 reaction. *Phys. Chem. Chem. Phys.* **16**, 19091–19105 (2014). Medline doi:10.1039/C4CP02593H

5. J. Lelieveld, T. M. Butler, J. N. Crowley, T. J. Dillon, H. Fischer, L. Ganzeveld, H. Harder, M. G. Lawrence, M. Martinez, D. Taraborrelli, J. Williams, Atmospheric oxidation capacity sustained by a tropical forest. *Nature* **452**, 737–740 (2008). Medline doi:10.1038/nature06870

6. R. L. Mauldin 3rd, T. Berndt, M. Sipilä, P. Paasonen, T. Petäjä, S. Kim, T. Kurtén, F. Stratmann, V. M. Kerminen, M. Kulmala, A new atmospherically relevant oxidant of sulphur dioxide. *Nature* **488**, 193–196 (2012). Medline doi:10.1038/nature11278

7. I. W. M. Smith, R. Zellner, Rate measurements of reactions of OH by resonance absorption. Part 2. Reactions of OH with CO, C_2H_4, and C_2H_2. *J. Chem. Soc., Faraday Trans. II* **69**, 1617–1627 (1973). doi:10.1039/F29736901617

8. J. Troe, Theory of thermal unimolecular reactions at high-pressures. *J. Chem. Phys.* **75**, 226–237 (1981). doi:10.1063/1.441829

9. D. Fulle, H. F. Hamann, H. Hippler, J. Troe, High pressure range of addition reactions of HO. II. Temperature and pressure dependence of the reaction HO+CO⇔HOCO→H+CO_2. *J. Chem. Phys.* **105**, 983–1000 (1996). doi:10.1063/1.471991

10. C. W. Larson, P. H. Stewart, D. M. Golden, Pressure and temperature-dependence of reactions proceeding via a bound complex. An approach for combustion and atmospheric chemistry modelers. Application to HO+CO → [HOCO] → H+CO_2. *Int. J. Chem. Kinet.* **20**, 27–40 (1988). doi:10.1002/kin.550200105

11. D. M. Golden, G. P. Smith, A. B. McEwen, B. Yu, B. Eiteneer, M. Frenklach, G. L. Vaghjiani, A. R. Ravishankara, F. P. Tully, OH(OD)+CO: Measurements and an optimized RRKM fit. *J. Phys. Chem. A* **102**, 8598–8606 (1998). doi:10.1021/jp982110m

12. D. C. McCabe, T. Gierczak, R. K. Talukdar, A. R. Ravishankara, Kinetics of the reaction OH plus CO under atmospheric conditions. *Geophys. Res. Lett.* **28**, 3135–3138 (2001). doi:10.1029/2000GL012719

13. G. Paraskevopoulos, R. S. Irwin, The pressure dependence of the rate constant of the reaction of OH radicals with CO. *J. Chem. Phys.* **80**, 259–266 (1984). doi:10.1063/1.446488

14. G. Paraskevopoulos, R. S. Irwin, The pressure-depdendence of the rate-constant of the reaction of OD radicals with CO. *Chem. Phys. Lett.* **93**, 138–143 (1982). doi:10.1016/0009-2614(82)83680-4

15. M. J. Frost, P. Sharkey, I. W. M. Smith, Energy and structure of the transition-states in the reaction OH+CO → H+CO_2. *Faraday Discuss.* **91**, 305–317 (1991). doi:10.1039/dc9919100305

16. M. J. Frost, P. Sharkey, I. W. M. Smith, Reaction between hydroxyl (deuteroxyl) radicals and carbon monoxide at temperatures down to 80 K: Experiment and theory. *J. Phys. Chem.* **97**, 12254–12259 (1993). doi:10.1021/j100149a027

17. J. Brunning, D. W. Derbyshire, I. W. M. Smith, M. D. Williams, Kinetics of OH(v= 0, 1) and OD(v= 0, 1) with CO and the mechanism of the OH + CO reaction. *J. Chem. Soc., Faraday Trans. II* **84**, 105–119 (1988). doi:10.1039/f29888400105

18. R. E. Weston Jr., T. L. Nguyen, J. F. Stanton, J. R. Barker, HO + CO reaction rates and H/D kinetic isotope effects: Master equation models with ab initio SCTST rate constants. *J. Phys. Chem. A* **117**, 821–835 (2013). Medline doi:10.1021/jp311928w

19. W. C. Chen, R. A. Marcus, On the theory of the CO plus OH reaction, including H and C kinetic isotope effects. *J. Chem. Phys.* **123**, 094307 (2005). doi:10.1063/1.2031208

20. C. H. Chang, G. T. Buckingham, D. J. Nesbitt, Sub-Doppler spectroscopy of the trans-HOCO radical in the OH stretching mode. *J. Phys. Chem. A* **117**, 13255–13264 (2013). Medline doi:10.1021/jp403386d

21. T. Oyama, W. Funato, Y. Sumiyoshi, Y. Endo, Observation of the pure rotational spectra of *trans*- and *cis*-HOCO. *J. Chem. Phys.* **134**, 174303 (2011). Medline doi:10.1063/1.3578179

22. M. C. McCarthy, O. Martinez Jr., B. A. McGuire, K. N. Crabtree, M. A. Martin-Drumel, J. F. Stanton, Isotopic studies of *trans*- and *cis*-HOCO using rotational spectroscopy: Formation, chemical bonding, and molecular structures. *J. Chem. Phys.* **144**, 124304 (2016). Medline doi:10.1063/1.4944070

23. A. J. Fleisher, B. J. Bjork, T. Q. Bui, K. C. Cossel, M. Okumura, J. Ye, Mid-infrared time-resolved frequency comb spectroscopy of transient free radicals. *J. Phys. Chem. Lett.* **5**, 2241–2246 (2014). Medline doi:10.1021/jz5008559

24. F. Adler, K. C. Cossel, M. J. Thorpe, I. Hartl, M. E. Fermann, J. Ye, Phase-stabilized, 1.5 W frequency comb at 2.8-4.8 microm. *Opt. Lett.* **34**, 1330–1332 (2009). Medline doi:10.1364/OL.34.001330

25. G. D. Cole, W. Zhang, B. J. Bjork, D. Follman, P. Heu, C. Deutsch, L. Sonderhouse, J. Robinson, C. Franz, A. Alexandrovski, M. Notcutt, O. H. Heckl, J. Ye, M. Aspelmeyer, High-performance near- and mid-infrared crystalline coatings. *Optica* **3**, 647–656 (2016). doi:10.1364/OPTICA.3.000647

26. J. C. Brock, R. T. Watson, Ozone photolysis: Determination of the O(^{3}P) quantum yield at 266 nm. *Chem. Phys. Lett.* **71**, 371–375 (1980). doi:10.1016/0009-2614(80)80185-0

27. J. E. Butler, R. G. Macdonald, D. J. Donaldson, J. J. Sloan, Vibrational-excitation of OH($X^2\Pi$) produced in the reaction of O(^{1}D) with H_2. *Chem. Phys. Lett.* **95**, 183–188 (1983). doi:10.1016/0009-2614(83)87228-5

28. M. Brouard, D. W. Hughes, K. S. Kalogerakis, J. P. Simons, The product rovibrational and spin–orbit state dependent dynamics of the complex reaction H+CO_2→ OH($^2\Pi$;v,N,Ω,f)+CO: Memories of a lifetime. *J. Chem. Phys.* **112**, 4557–4571 (2000). doi:10.1063/1.481081

29. N. Kohno, M. Izumi, H. Kohguchi, K. Yamasaki, Acceleration of the reaction OH + CO → H + CO_2 by vibrational excitation of OH. *J. Phys. Chem. A* **115**, 4867–4873 (2011). Medline doi:10.1021/jp200220f

30. N. F. Scherer, L. R. Khundkar, R. B. Bernstein, A. H. Zewail, Real-time picosecond clocking of the collision complex in a bimolecular reaction: The birth of OH from H+CO_2. *J. Chem. Phys.* **87**, 1451–1453 (1987). doi:10.1063/1.453280

31. S. I. Ionov, G. A. Brucker, C. Jaques, L. Valachovic, C. Wittig, Subpicosecond resolution studies of the H+CO_2→CO+OH reaction photoinitiated in CO_2-HI complexes. *J. Chem. Phys.* **99**, 6553–6561 (1993). doi:10.1063/1.465847

32. D. C. Clary, G. C. Schatz, Quantum and quasi-classical calculations on the OH+CO→CO_2+H reaction. *J. Chem. Phys.* **99**, 4578–4589 (1993). doi:10.1063/1.466057

33. M. I. Hernández, D. C. Clary, A study of HOCO resonances in the OH+CO→CO_2+H reaction. *J. Chem. Phys.* **101**, 2779–2784 (1994). doi:10.1063/1.467593

34. C. Western, PGOPHER, A Program for Simulating Rotational, Vibrational and Electronic Spectra, *J. Quant. Spectro. Rad. Transfer* 10.1016/j.jqsrt.2016.04.010 (2016).

35. J. T. Petty, C. B. Moore, Transient infrared-absorption spectrum of the ν1 fundamental of *trans*-DOCO. *J. Chem. Phys.* **99**, 47–55 (1993). doi:10.1063/1.465773

36. M. C. Abrams, S. P. Davis, M. L. P. Rao, R. Engleman, High-resolution Fourier-transform spectroscopy of the vibration-rotation spectrum of the OD radical. *J. Mol. Spectrosc.* **165**, 57–74 (1994). doi:10.1006/jmsp.1994.1110

37. R. A. Toth, HDO and D_2O low pressure, long path spectra in the 600–3100 cm^{-1} region. *J. Mol. Spectrosc.* **195**, 98–122 (1999). Medline doi:10.1006/jmsp.1999.7815

38. Y. Liu, S. P. Sander, Rate constant for the OH + CO reaction at low temperatures. *J. Phys. Chem. A* **119**, 10060–10066 (2015). Medline doi:10.1021/acs.jpca.5b07220

39. A. A. Westenberg, W. E. Wilson, ESR intensity relations and some gas-phase chemical kinetics of the OD radical. *J. Chem. Phys.* **45**, 338–342 (1966). doi:10.1063/1.1727330

40. C. S. Boxe, J. S. Francisco, Y. L. Shia, Y. L. Yung, H. Nair, M.-C. Liang, A. Saiz-Lopez, Yung, H. Nair, Liang, A. Saiz-Lopez, New insights into martian atmospheric chemistry. *Icarus* **242**, 97–104 (2014). doi:10.1016/j.icarus.2014.07.023

41. J. B. Burkholder, S. P. Sander, J. P. D. Abbatt, J. R. Barker, R. E. Huie, C. E. Kolb, M. J. Kurylo, V. L. Orkin, D. M. Wilmouth, P. H. Wine, "Chemical kinetics and photochemical data for use in atmospheric studies, evaluation no. 18" (JPL Publication 15-10, Jet Propulsion Laboratory, 2015).

42. R. A. Toth, Air- and N_2-broadening parameters of HDO and D_2O, 709 to 1936 cm^{-1}. *J. Mol. Spectrosc.* **198**, 358–370 (1999). Medline doi:10.1006/jmsp.1999.7966

43. D. D. Nelson, A. Schiffman, D. J. Nesbitt, The dipole-moment function and vibrational transition intensities of OH. *J. Chem. Phys.* **90**, 5455–5465 (1989). doi:10.1063/1.456451

44. D. D. Nelson, A. Schiffman, D. J. Nesbitt, D. J. Yaron, Absolute infrared transition moments for open-shell diatomics from *J* dependence of transition intensities. Application to OH. *J. Chem. Phys.* **90**, 5443–5454 (1989). doi:10.1063/1.456450

45. M. J. Thorpe, J. Ye, Cavity-enhanced direct frequency comb spectroscopy. *Appl. Phys. B* **91**, 397–414 (2008). doi:10.1007/s00340-008-3019-1

46. J. E. Butler, G. M. Jursich, I. A. Watson, J. R. Wiesenfeld, Reaction dynamics of $O(^1D_2)$ + H_2, HD, D_2: OH, OD($X\ 2\Pi_i$) product internal energy distributions. *J. Chem. Phys.* **84**, 5365–5377 (1986). doi:10.1063/1.449947

47. G. E. Streit, H. S. Johnston, Reactions and quenching of vibrationally excited hydroxyl radicals. *J. Chem. Phys.* **64**, 95–103 (1976). doi:10.1063/1.431917

48. B. M. Toselli, J. D. Brenner, M. L. Yerram, W. E. Chin, K. D. King, J. R. Barker, Vibrational-relaxation of highly excited toluene. *J. Chem. Phys.* **95**, 176–188 (1991). doi:10.1063/1.461473

49. J. C. Ianni, Kintecus, Windows Version 2.80 (2002).

50. A. R. Ravishankara, E. J. Dunlea, M. A. Blitz, T. J. Dillon, D. E. Heard, M. J. Pilling, R. S. Strekowski, J. M. Nicovich, P. H. Wine, Redetermination of the rate coefficient for the reaction of $O(^1D)$ with N_2. *Geophys. Res. Lett.* **29**, 4 (2002).

51. J. A. Davidson, H. I. Schiff, T. J. Brown, C. J. Howard, Temperature-dependence of deactivation of $O(^1D)$ by CO from 113-333 K. *J. Chem. Phys.* **69**, 1216–1217 (1978). doi:10.1063/1.436657

52. M. A. Blitz, T. J. Dillon, D. E. Heard, M. J. Pilling, I. D. Trought, Laser induced fluorescence studies of the reactions of $O(^1D_2)$ with N_2, O_2, N_2O, CH_4, H_2, CO_2, Ar, Kr and *n*-C_4H_{10}. *Phys. Chem. Chem. Phys.* **6**, 2162–2171 (2004). doi:10.1039/b400283k

53. R. K. Talukdar, A. R. Ravishankara, Rate coefficients for $O(^1D)$+H_2, D_2, HD reactions and H atom yield in $O(^1D)$+HD reaction. *Chem. Phys. Lett.* **253**, 177–183 (1996). doi:10.1016/0009-2614(96)00203-5

54. L. P. Ju, K. L. Han, A. J. C. Varandas, Variational transition-state theory study of the atmospheric reaction OH+O_3 → HO_2+O_2. *Int. J. Chem. Kinet.* **39**, 148–153 (2007). doi:10.1002/kin.20226

55. R. K. Talukdar, T. Gierczak, L. Goldfarb, Y. Rudich, B. S. M. Rao, A. R. Ravishankara, Kinetics of hydroxyl radical reactions with isotopically labeled hydrogen. *J. Phys. Chem.* **100**, 3037–3043 (1996). doi:10.1021/jp9518724

56. Y. Bedjanian, G. Le Bras, G. Poulet, Kinetic study of OH plus OH and OD plus OD reactions. *J. Phys. Chem. A* **103**, 7017–7025 (1999). doi:10.1021/jp991146r

57. Y. Bedjanian, V. Riffault, G. Le Bras, G. Poulet, Kinetics and mechanism of the OH and OD reactions with BrO. *J. Phys. Chem. A* **105**, 6154–6166 (2001). doi:10.1021/jp010369q

58. G. L. Vaghjiani, A. R. Ravishankara, N. Cohen, Reactions of hydroxyl and hydroxyl-D with hydrogen peroxide and hydrogen peroxide-D_2. *J. Phys. Chem.* **93**, 7833–7837 (1989). doi:10.1021/j100360a021

59. H. G. Yu, J. S. Francisco, Energetics and kinetics of the reaction of HOCO with hydrogen atoms. *J. Chem. Phys.* **128**, 244315 (2008). Medline doi:10.1063/1.2946696

60. H. G. Yu, J. T. Muckerman, J. S. Francisco, Direct ab initio dynamics study of the OH + HOCO reaction. *J. Phys. Chem. A* **109**, 5230–5236 (2005). Medline doi:10.1021/jp051458w

61. H. G. Yu, J. T. Muckerman, J. S. Francisco, Quantum force molecular dynamics study of the reaction of O atoms with HOCO. *J. Chem. Phys.* **127**, 094302 (2007). Medline doi:10.1063/1.2770463

62. J. T. Petty, J. A. Harrison, C. B. Moore, Reactions of *trans*-hydroxycarbonyl radical studied by infrared spectroscopy. *J. Phys. Chem.* **97**, 11194–11198 (1993). doi:10.1021/j100145a013